




Nonadiabatic geometric quantum gates by composite pulses based on superconducting qubits

Zi-Yu Fang ^{1,2,*} Hai Xu ^{1,2,*} Tao Chen,^{3,4,†} Kejin Wei,^{1,2} and Chengxian Zhang ^{1,2,‡}

¹*School of Physical Science and Technology, Guangxi University, Nanning 530004, China*

²*Guangxi Key Laboratory for Relativistic Astrophysics, School of Physical Science and Technology, Guangxi University, Nanning 530004, China*

³*Key Laboratory of Atomic and Subatomic Structure and Quantum Control (Ministry of Education), School of Physics, South China Normal University, Guangzhou 510006, China*

⁴*Guangdong Provincial Key Laboratory of Quantum Engineering and Quantum Materials, Guangdong-Hong Kong Joint Laboratory of Quantum Matter, Frontier Research Institute for Physics, South China Normal University, Guangzhou 510006, China*



(Received 23 November 2023; accepted 18 March 2024; published 11 April 2024)

The nonadiabatic geometric quantum gate (NGQG) is promising for the realization of high-fidelity operation for large-scale quantum processing. Normally, conventional NGQGs can be especially robust to either the Rabi error or the detuning error, which are two typical errors in many quantum computing platforms. However, it is difficult to suppress these two types of errors at the same time. This remains a big challenge for NGQGs. Here we present a general framework to implement the optimized geometric gate, where the evolution path is performed by using a family of optimized composite pulses. These composite pulses can reduce the sensitivity to the detuning error without introducing an extra Rabi error for this path. Thus, they help fulfill the cyclic evolution condition for the geometric gate. In addition, the inserted composite pulses would not introduce unwanted dynamical phase accumulation. As a result, the designed optimized geometric gate can simultaneously mitigate both the Rabi and detuning errors even in the presence of decoherence related to the real experiments. Our work paves a way to achieve geometric quantum computation robust against multiple errors.

DOI: [10.1103/PhysRevA.109.042615](https://doi.org/10.1103/PhysRevA.109.042615)

I. INTRODUCTION

Fault-tolerant quantum computation demands high-precision manipulation for large-scale quantum processing. However, when implementing the gate operations in specific platforms, errors existing in the control environment substantially reduce the control fidelity. In addition, considering decoherence effects, the case would become worse. In order to realize high-fidelity quantum computation, many methods have been proposed to mitigate the gate errors, such as the composite pulse sequences [1–4], time optimal control [5–10], and designing gates using geometric space curves [11–14]. Nevertheless, many of them implement gates by using the dynamical phase, which correlates with the energy of the Hamiltonian. Geometric quantum computation (GQC) [15,16] based on the geometric phase is believed to be a great choice to avoid the influence of quantum gate errors. Compared to conventional dynamical phase, the geometric phase is inherently robust to certain types of local error, since it only depends on the global property of the evolution. Therefore, it can ignore the evolution details during evolution [17–21].

In the early development of GQC, the geometric gate was designed using the Berry phase [19], which is obtained for

the quantum state after adiabatic and cyclic evolution. This hinders the use of GQC in real experiments due to slow adiabatic evolution when considering decoherence [16,22,23]. In order to overcome this adiabatic limitation, a nonadiabatic geometric quantum gate (NGQG) based on the nonadiabatic geometric phase, i.e., the Aharonov-Anandan phase, was proposed to speed up the gate time [24,25]. The NGQG has been studied theoretically and experimentally in many systems, such as superconducting circuits [26–30], trapped ions [31,32], the nitrogen-vacancy center in diamond [33–35], and NMR [36–38]. In fact, the conventional NGQG is especially useful in suppressing the Rabi error [39–45], which is induced by the inaccurate control of the Rabi frequency; however, it is hard to deal with the detuning error at the same time [46–48]. The detuning error is the dominant error source in many platforms, such as the superconducting circuit and silicon quantum dot. In the past, in combination with other techniques, various NGQGs have been proposed to enhance the robustness for conventional NGQGs. For example, a robust NGQG can be made by using the optimal control technique [49–55], the dynamical decoupling method [56–59], or the reverse engineering scheme [60–62]. Most of these schemes can be rather effective in combatting the Rabi error; however, they can always lead to a poor performance when considering the detuning error simultaneously. In Refs. [46–48] it was found that by picking up different evolution loops, the obtained geometric gate can be more robust to the detuning error compared to the dynamical gate. However, this would substantially weaken the ability to mitigate the Rabi error.

*These authors contributed equally to this work.

†chentamail@163.com

‡cxzhang@gxu.edu.cn

Recently, it was also found that by combining the geometric phase and the geometric space curves, it is possible to obtain the so-called doubly geometric quantum control that can implement z -axis rotation [11]. In Ref. [11] both the detuning and Rabi errors could be suppressed at the same time. On the other hand, in Ref. [11], except for the Rabi driving field, one still needs to synchronously drive the detuning field, which increases the complexity of the experiments. Therefore, how to simultaneously mitigate these two types of errors and obtain the universal gate operations still remains a challenge for NGQGs.

In this work we propose theoretically a general method to implement universal optimized NGQGs. The optimized NGQG is performed by using an optimized set of composite pulses [4] to refine the evolution path. In contrast to the conventional NGQG scheme, these introduced composite pulses would not introduce an extra Rabi error for the path. Meanwhile, they can reduce the sensitivity to detuning error. As a result, the composite pulses help fulfill the cyclic evolution condition for the geometric gate, and the implemented optimized NGQG can mitigate both the Rabi error and detuning error at the same time. In addition, in the implementation of the optimized NGQG, we always shut down the detuning field, i.e., $\Delta(t) \equiv 0$. This also makes the optimized NGQG adaptable to experiments. It is demonstrated that the inserted composite pulses would not introduce the dynamical phase accumulation during the whole operation. We verify the performance of our optimized geometric gates (including a universal set of single- and two-qubit gates) via implementing them in the superconducting transmon qubits, considering the errors and decoherence level related to the real experiments. Although the evolution time for the optimized geometric gate is prolonged, it can still outperform the dynamical gates. It is worth noting that whether the proposed optimized geometric gate can still offer a better performance than the dynamical gates in other platforms remains a question for further study.

II. GEOMETRIC QUANTUM GATE BASED ON PATH DESIGN

In this section we first propose the general framework to implement the geometric gate via inverse engineering. Based on this framework, we further discuss how to improve the conventional geometric gate through composite pulses for path optimization.

A. General geometric quantum gate via inverse engineering

Consider a general two-level system driven by an external microwave field [41,42,46] whose Hamiltonian in the computational basis $|0\rangle$ and $|1\rangle$ can be described as

$$\mathcal{H}(t) = \frac{1}{2} \begin{pmatrix} -\Delta(t) & \Omega(t)e^{-i\varphi(t)} \\ \Omega(t)e^{i\varphi(t)} & \Delta(t) \end{pmatrix}, \quad (1)$$

where $\Omega(t)$ and $\varphi(t)$ are the time-dependent amplitude and phase of the driving field, respectively, and $\Delta(t)$ is the time-dependent detuning field due to the frequency difference between the qubit transition energy and the microwave field. Hereafter, we set $\hbar = 1$ for simplicity.

It is convenient to describe the geometric gate by using the evolution of a pair of orthogonal states, i.e., the dressed-state basis, which are defined as

$$\begin{aligned} |\Psi_+(t)\rangle &= \cos \frac{\theta(t)}{2} |0\rangle + \sin \frac{\theta(t)}{2} e^{i\phi(t)} |1\rangle, \\ |\Psi_-(t)\rangle &= \sin \frac{\theta(t)}{2} e^{-i\phi(t)} |0\rangle - \cos \frac{\theta(t)}{2} |1\rangle. \end{aligned} \quad (2)$$

Here, if we treat $|\Psi_{\pm}(t)\rangle$ as the qubit states on the Bloch sphere, $\theta(t)$ and $\phi(t)$ can be regarded as the polar angle and azimuthal angle of the spherical coordinates, respectively. The angles $\theta(t)$ and $\phi(t)$ can be determined by solving the von Neumann equation [46,49]

$$\frac{\partial}{\partial t} [|\Psi_{\pm}(t)\rangle\langle\Psi_{\pm}(t)|] = -i[\mathcal{H}(t), |\Psi_{\pm}(t)\rangle\langle\Psi_{\pm}(t)|]. \quad (3)$$

Then we can obtain

$$\begin{aligned} \dot{\phi}(t) &= -\Delta(t) - \Omega(t) \cot \theta(t) \cos[\varphi(t) - \phi(t)], \\ \dot{\theta}(t) &= \Omega(t) \sin[\varphi(t) - \phi(t)]. \end{aligned} \quad (4)$$

The parameters in the control Hamiltonian $\mathcal{H}(t)$ can be inversely determined from Eq. (4) as

$$\begin{aligned} \Omega(t) &= \pm \sqrt{(\Delta - \dot{\phi})^2 + \dot{\theta}^2 \cot^2 \theta \tan \theta}, \\ \varphi(t) &= \theta - \arctan \left(\pm \frac{\dot{\theta} \cot \theta}{\Delta - 2\dot{\theta}} \right). \end{aligned} \quad (5)$$

On the other hand, by driving the appropriate parameters $\{\Omega(t), \varphi(t)\}$ in $\mathcal{H}(t)$, the evolution of the two dressed states can be easily controlled. In particular, after tracing out closed loops on the Bloch sphere at the final time τ , the cyclic evolution condition of the dressed states for the geometric gate would be satisfied [42,48], either of which would obtain a global phase factor $|\Psi_{\pm}(\tau)\rangle = e^{i\gamma_{\pm}} |\Psi_{\pm}(0)\rangle$, with $\gamma_+ = -\gamma_- = \gamma$. In this way, the obtained evolution operator can be written as

$$U(\tau) = e^{i\gamma} |\Psi_+(0)\rangle\langle\Psi_+(0)| + e^{-i\gamma} |\Psi_-(0)\rangle\langle\Psi_-(0)|. \quad (6)$$

Note that the accumulated total phase factor generally can be divided into two parts, i.e., the dynamical phase γ_d and the geometric phase γ_g . The key to implementing a geometric gate is to cancel out the dynamical phase and retain the pure geometric one. By inserting Eq. (4) into the definition of the dynamical phase, the dynamical and geometric phases can be parametrized as

$$\gamma_d = - \int_0^{\tau} \langle\Psi_+(t)|\mathcal{H}(t)|\Psi_+(t)\rangle dt \quad (7a)$$

$$= \frac{1}{2} \int_0^{\tau} \frac{\dot{\phi}(t) \sin^2 \theta(t) + \Delta(t)}{\cos \theta(t)} dt, \quad (7b)$$

$$\gamma_g = \gamma - \gamma_d. \quad (7c)$$

According to Eq. (7b), for the case of $\Delta(t) \equiv 0$, namely, when the qubit is on resonance with the microwave field, the dynamical phase cancels out when taking $\dot{\phi}(t) = 0$. This means the dressed state evolves along a certain longitude line on the Bloch sphere. In addition, the global phase factor is

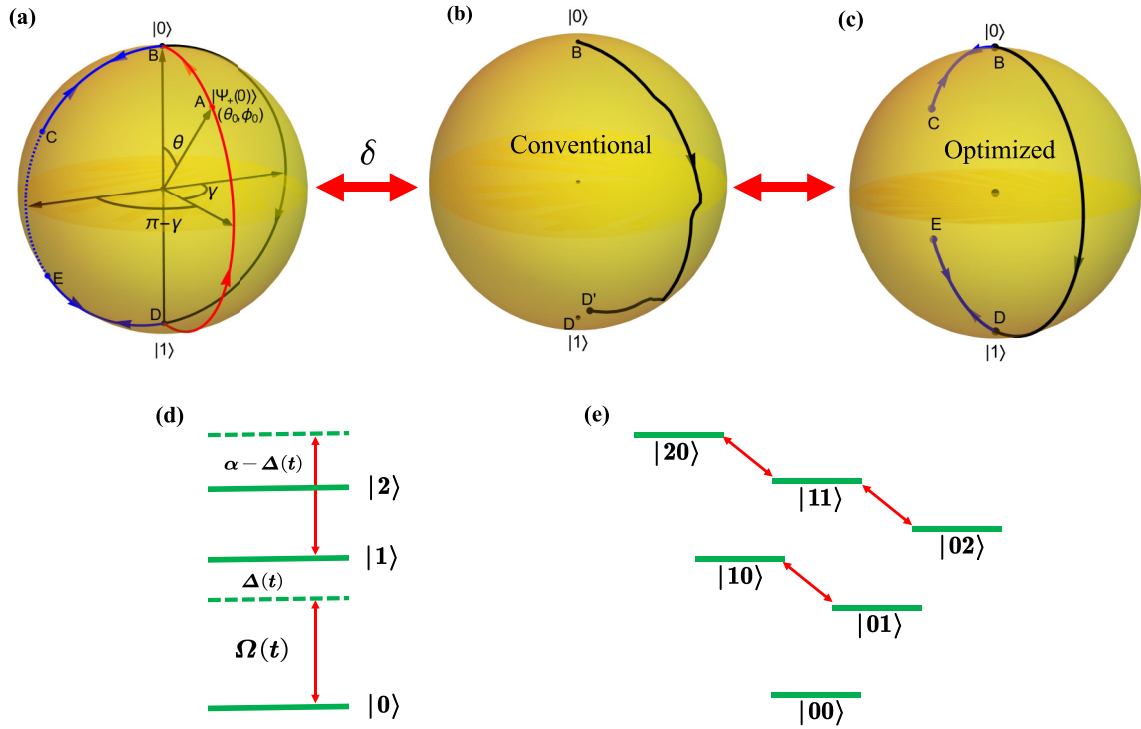


FIG. 1. (a) Evolution trajectory of the dressed state $|\Psi_+(t)\rangle$. For the conventional NGQG, it evolves along the path $A \rightarrow B \rightarrow D \rightarrow A$ to enclose the so-called orange-slice shape, while for the optimized geometric gate, it evolves along the path $A \rightarrow B \rightarrow C \rightarrow B \rightarrow D \rightarrow E \rightarrow D \rightarrow A$ to fulfill cyclic evolution. (b) For the conventional NGQG, the dressed state from the north pole cannot evolve to the south pole in the presence of detuning error. (c) For the optimized geometric gates, the composite pulses helps the dressed state reach the south pole in the presence of detuning error. (d) Energy level of a transmon qubit, the two lowest levels ($|0\rangle$ and $|1\rangle$) of which are used to encode a single qubit and the third level $|2\rangle$ is regarded as the main leakage source due to the weak anharmonicity in the transmon qubit. (e) Energy-level diagram for two coupled transmon qubits, where the single-excitation subspace $\{|10\rangle, |01\rangle\}$ can be used to implement the optimized geometric isWQG gate.

thus the pure geometric phase $\gamma = \gamma_g$. Note that the azimuthal angle $\phi(t)$ at the north or south pole is discontinuous. Thus, the derivatives $\dot{\phi}(t)$ at these points are nonzero and might be indeterminate. In this way, one should calculate the dynamical phase by directly using the definition in Eq. (7a) instead of the parametrized expression in Eq. (7b). In Appendix B we demonstrate that even though $\phi(t)$ jumps at these discontinuity points, the dynamical phases accumulated are still zero.

B. Conventional geometric quantum gate

The typical conventional NGQG [42,43,46,47] is as shown in Fig. 1(a), the basic idea of which is to evolve the dressed state always along a specific longitude so as to enclose the so-called orange-slice loop. For any designed geometric gate, the whole evolution path is divided into three segments. As one can see, the initial dressed state $|\Psi_+(0)\rangle$ on the Bloch sphere starts from a certain point A with coordinate (θ_0, ϕ_0) (determined by the specific gate operation, as seen below) and travels to the north pole B along the longitude denoted by the red A-B path. During the second evolution process, it goes right down to the south pole D along another longitude denoted by the gray B-D path. Finally, the dressed state returns to the original point along the D-A path. In such a way, the dressed state fulfills a cyclic evolution $A \rightarrow B \rightarrow D \rightarrow A$. For this evolution loop, one can easily derive its control

Hamiltonian parameters via Eq. (5). During each time interval, the parameters satisfy

$$\int_0^{T_1} \Omega(t) dt = \theta_0 \left\{ \varphi(t) \equiv \varphi_g^1 = \phi_0 - \frac{\pi}{2}, t \in [0, T_1] \right\}, \quad (8a)$$

$$\int_{T_1}^{T_2} \Omega(t) dt = \pi \left\{ \varphi(t) \equiv \varphi_g^2 = \phi_0 + \gamma + \frac{\pi}{2}, t \in [T_1, T_2] \right\}, \quad (8b)$$

$$\int_{T_2}^T \Omega(t) dt = \pi - \theta_0 \left\{ \varphi(t) \equiv \varphi_g^3 = \phi_0 - \frac{\pi}{2}, t \in [T_2, T] \right\}. \quad (8c)$$

Meanwhile, we have $\Delta \equiv 0$ during the gate operation. The resulting geometric operator is thus

$$\begin{aligned} U_g(T) &= U_{DA}(T, T_2) U_{BD}(T_2, T_1) U_{AB}(T_1, 0) \\ &= \cos \gamma \hat{I} + i \sin \gamma \begin{pmatrix} \cos \theta_0 & \sin \theta_0 e^{-i\phi_0} \\ \sin \theta_0 e^{i\phi_0} & -\cos \theta_0 \end{pmatrix} \\ &= e^{i\gamma \vec{n} \cdot \vec{\sigma}}, \end{aligned} \quad (9)$$

where $\vec{n} = (\sin \theta_0 \cos \phi_0, \sin \theta_0 \sin \phi_0, \cos \theta_0)$ can be regarded as the unit vector on the Bloch sphere. By setting appropriate

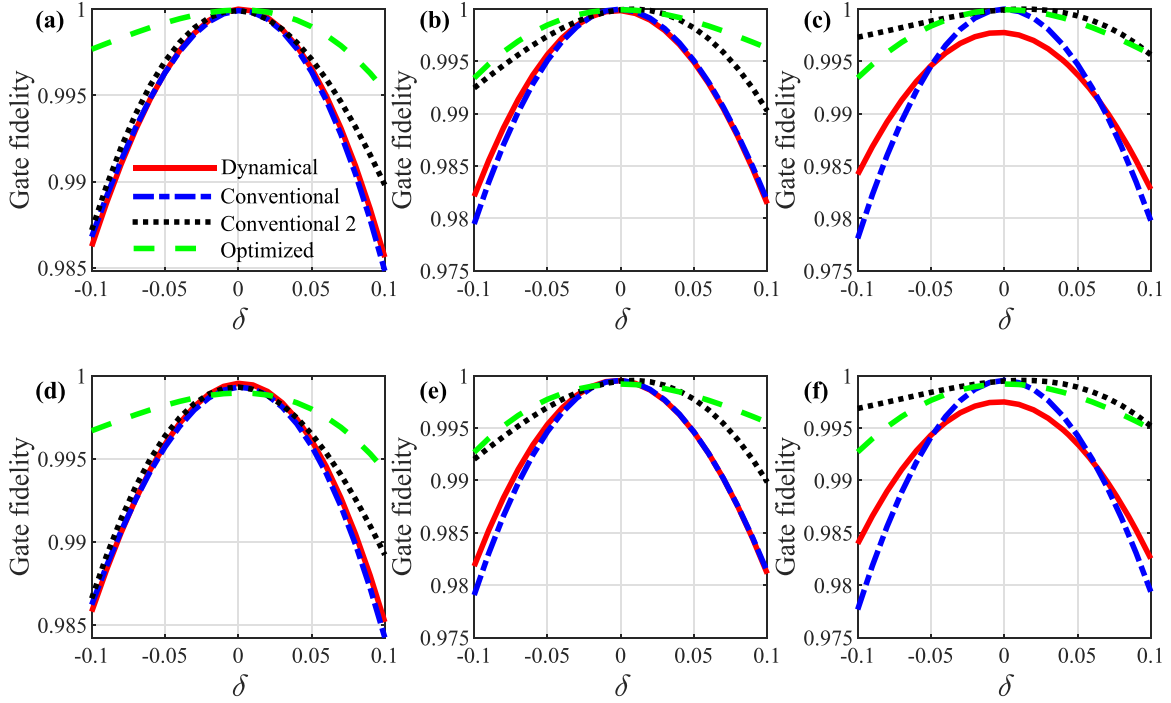


FIG. 2. Gate fidelity versus detuning error δ , where the Rabi error is zero, i.e., $\epsilon = 0$, and the decoherence rate is (a)–(c) $\kappa = 0$ and (d)–(f) $\kappa = 2\pi \times 4$ kHz, for the (a) and (d) H , (b) and (e) S , and (c) and (f) T gates. Conventional refers to the geometric gate as shown in Eq. (8), conventional 2 refers to the scheme as shown in Refs. [46,47], and optimized refers to the gate parameters in Eq. (15).

parameters $\{\gamma, \theta_0, \phi_0\}$, $U_g(T)$ can implement arbitrary single-qubit rotation, namely, it is universal.

On the other hand, the operator can be alternatively written as

$$U_g(T) = |\Psi_+(T)\rangle\langle\Psi_+(0)| + |\Psi_-(T)\rangle\langle\Psi_-(0)| \\ = e^{i\gamma}|\Psi_+(0)\rangle\langle\Psi_+(0)| + e^{-i\gamma}|\Psi_-(0)\rangle\langle\Psi_-(0)|. \quad (10)$$

It is clear that $|\Psi_+(t)\rangle$ ($|\Psi_-(t)\rangle$) fulfills the cyclic evolution condition at the final evolution time T [determined by $\int_0^T \Omega(t)dt = 2\pi$] and obtains a corresponding global phase factor γ ($-\gamma$). According to the parameters in Eqs. (8), the related azimuthal angle during each path reads

$$\phi(t) = \begin{cases} \phi_0, & A \rightarrow B \\ \phi_0 + \gamma, & B \rightarrow D \\ \phi_0, & D \rightarrow A. \end{cases} \quad (11)$$

It is clear that except for the discontinuous points B and D , we have $\dot{\phi}(t) = 0$, and the accumulated dynamical phase in the whole evolution process is zero, as mentioned above. Meanwhile, the obtained global phase factor γ represents the pure geometric phase and $U_g(T)$ is a pure geometric quantum gate.

In the implementation of gate operations, the control Hamiltonian can suffer from mainly two types of errors, i.e., the detuning and Rabi errors. The corresponding control Hamiltonian can be written as

$$H'_c(t) = \frac{(1 + \epsilon)\Omega(t)}{2} [\cos \varphi(t)\sigma_x + \sin \varphi(t)\sigma_y] - \frac{\Omega(t)\delta}{2}\sigma_z. \quad (12)$$

Here ϵ and δ denote the Rabi and detuning errors, respectively. It is worth noting that, in this work, we treat these two errors as perturbations, which is normally reasonable considering $|\epsilon|, |\delta| \ll \Omega_{\max}$. The robustness of the conventional geometric gate against detuning errors is shown in Fig. 2. Here we consider the universal single-qubit gate set $\{H, S, T\}$. The robustness for other types of gates is shown in Appendix A. It is clear that the conventional geometric gates [see the blue long-dash-short-dashed lines in Figs. 2(a)–2(c)] perform even worse than the dynamical gates (solid red lines), which is directly designed using the control Hamiltonian in Eq. (12). However, from Figs. 3(a)–3(c) we also see that it can effectively combat the Rabi error. Therefore, the detuning error is the dominant error source for the conventional NGQG. To suppress the detuning error, one can alternatively construct the geometric gate by designing another evolution path [46,47] during the second time interval, namely, $(\varphi_g^2)' \equiv \varphi_g^2 - \pi$, $t \in [T_1, T_2]$. In contrast, this type of geometric gate (see the black dotted lines) would be robust to the detuning error while it is rather susceptible to the Rabi error. For simplicity, we denote the geometric gates in Refs. [46,47] as conventional 2 NGQG. Both types of NGQGs cannot simultaneously mitigate these two types of errors.

C. Optimized geometric quantum gates based on composite pulses

As stated above, the conventional NGQG is robust to the Rabi error while it is sensitive to the detuning error. Therefore, the key to optimizing the conventional NGQG is to combat the detuning error during the evolution. In fact, for arbitrary gate operation based on conventional NGQGs, the dressed

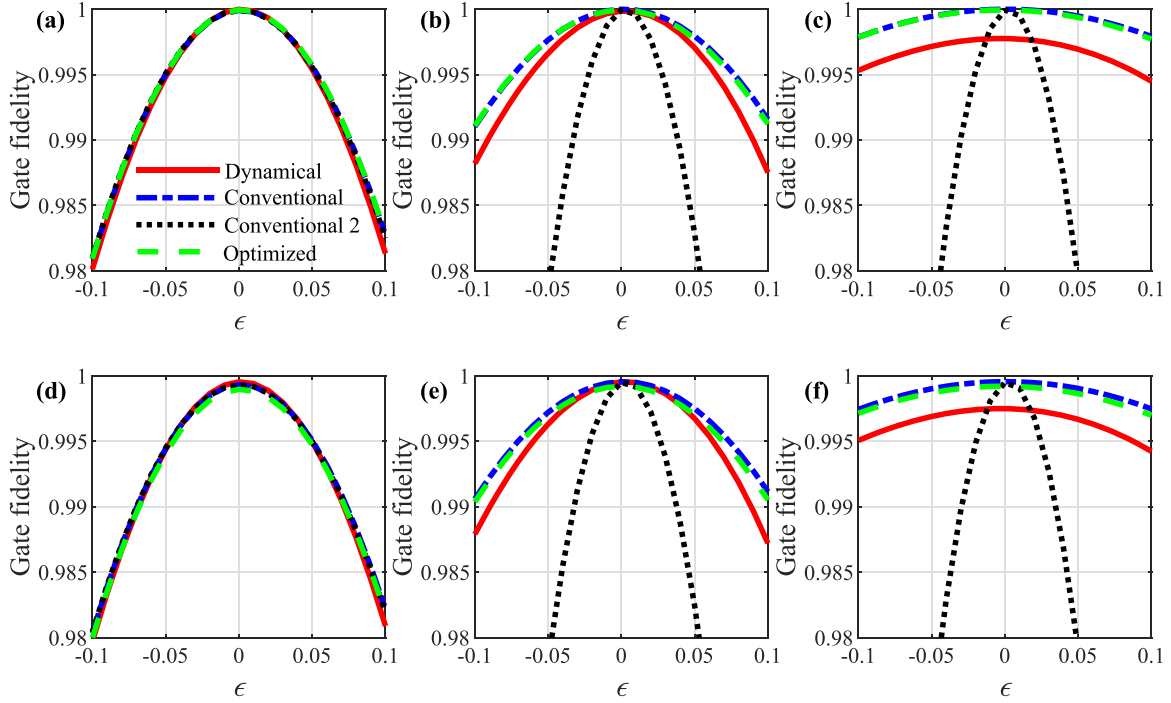


FIG. 3. Gate fidelity versus Rabi error ϵ , where the detuning error is zero, i.e., $\delta = 0$, and the decoherence rate is (a)–(c) $\kappa = 0$ and (d)–(f) $\kappa = 2\pi \times 4$ kHz, for the (a) and (d) H , (b) and (e) S , and (c) and (f) T gates. Conventional refers to the geometric gate as shown in Eq. (8), conventional 2 refers to the scheme as shown in Refs. [46,47], and optimized refers to the gate parameters in Eq. (15).

state would go through the longitude from the north pole B to the south pole D [see Fig. 1(b)], which corresponds to the second evolution $U_{BD}(T_2, T_1)$. Actually, the ideal evolution operator corresponding to $U_{BD}(T_2, T_1)$ can be regarded as a π rotation

$$\begin{aligned} R(\pi, \varphi_g^2) &= \exp\left(-i \int_{T_1}^{T_2} \frac{\Omega(t)}{2} (\cos \varphi_g^2 \sigma_x + \sin \varphi_g^2 \sigma_y) dt\right) \\ &= \exp\left(-i \frac{\pi}{2} (\cos \varphi_g^2 \sigma_x + \sin \varphi_g^2 \sigma_y)\right) \end{aligned} \quad (13)$$

around a specific axis determined by φ_g^2 on the x - y plane. As shown in Fig. 1(b), in the presence of detuning error, the dressed state would deviate from the south pole and reach another point D' . Thus, we have $U_{BD}(T_2, T_1) \neq R(\pi, \varphi_g^2)$ and $|\Psi_{+,D}^\delta\rangle \neq |\Psi_{+,D}\rangle$ with $|\Psi_{+,D}\rangle = R(\pi, \varphi_g^2)|0\rangle$. It is obvious that the dressed state cannot go back to the starting point to fulfill cyclic evolution.

To optimize the conventional NGQG, we should refine the evolution path, where the path itself is robust to the detuning error. This can be achieved by using an optimized composite pulse based on the identity

$$R(\pi, \varphi_g^2) = R\left(\frac{\pi}{3}, \varphi_{\text{opt}}^4\right) R\left(\frac{5\pi}{3}, \varphi_{\text{opt}}^3\right) R\left(\frac{\pi}{3}, \varphi_{\text{opt}}^2\right). \quad (14)$$

Here $\varphi_{\text{opt}}^2 = \varphi_{\text{opt}}^4 = \varphi_g^2 + \pi$ and $\varphi_{\text{opt}}^3 = \varphi_g^2$, which are determined by φ_g^2 . We now explain why the optimized composite π pulse is more robust than the original one based on the conventional NGQG. To quantitatively compare these two types of π pulses, we define the infidelity as $\delta F = 1 - |\langle \Psi_{+,D}^\delta | \Psi_{+,D} \rangle|^2$. As shown in Fig. 4(a), compared to the original π pulse

represented by $U_{BD}(T_2, T_1)$, the infidelity for the optimized one in Eq. (14) is much lower in the whole detuning error region considered $\delta \in [-0.1, 0.1]$. In addition, optimized composite π pulse would not introduce extra infidelity when considering the Rabi error, as shown in Fig. 4(b). As a result in Fig. 1(c), the dressed state can evolve to the south pole even though the detuning error exists. Further, it helps to fulfill all the cyclic evolution.

By inserting this composite π pulse into Eq. (8b) and keeping the other two evolutions in Eqs. (8a) and (8c) unchanged, we can realize an arbitrary optimized geometric gate. The corresponding parameters for the Hamiltonian during each part satisfy

$$\int_0^{T_1} \Omega(t) dt = \theta_0 \quad \{\varphi(t) \equiv \varphi_{\text{opt}}^1 = \varphi_g^1, t \in [0, T_1]\}, \quad (15a)$$

$$\int_{T_1}^{T_2} \Omega(t) dt = \frac{\pi}{3} \quad \{\varphi(t) \equiv \varphi_{\text{opt}}^2, t \in [T_1, T_2]\}, \quad (15b)$$

$$\int_{T_2}^{T_3} \Omega(t) dt = \frac{5\pi}{3} \quad \{\varphi(t) \equiv \varphi_{\text{opt}}^3, t \in [T_2, T_3]\}, \quad (15c)$$

$$\int_{T_3}^{T_4} \Omega(t) dt = \frac{\pi}{3} \quad \{\varphi(t) \equiv \varphi_{\text{opt}}^4, t \in [T_3, T_4]\}, \quad (15d)$$

$$\int_{T_4}^T \Omega(t) dt = \pi - \theta_0 \quad \{\varphi(t) \equiv \varphi_{\text{opt}}^5 = \varphi_g^3, t \in [T_4, T]\}. \quad (15e)$$

Also, we have $\Delta \equiv 0$ during the whole evolution. At the end of the evolution time, namely, $\int_0^T \Omega(t) dt = \frac{10\pi}{3}$, the resultant

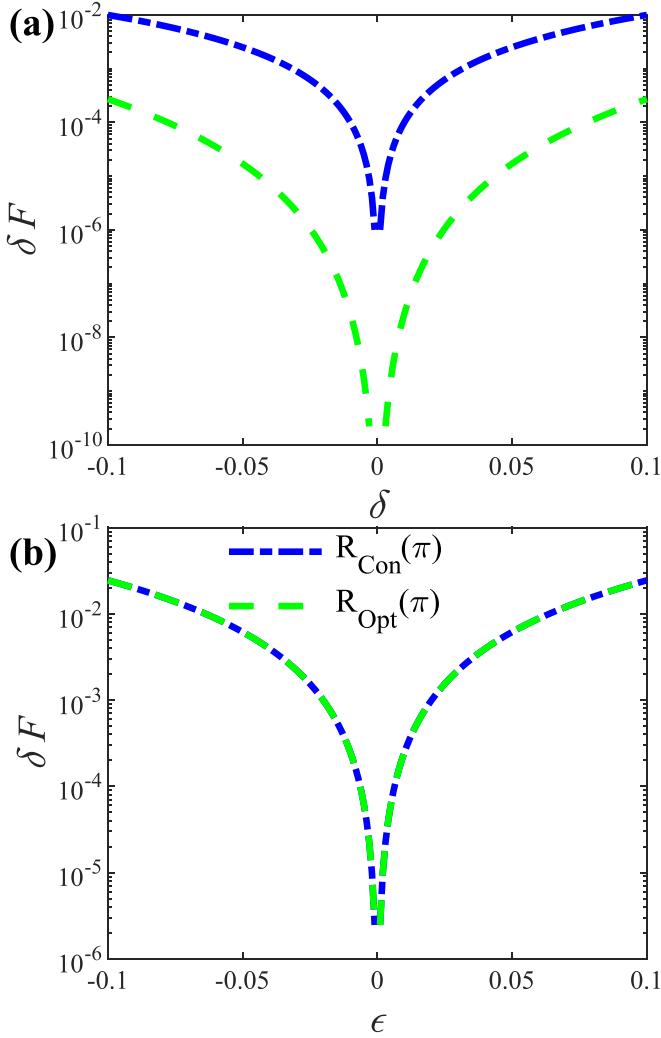


FIG. 4. Infidelity for the effective π pulse which corresponds to the evolution operator $U_{BD}(T_2, T_1)$ (blue long-dash–short-dashed lines) in conventional NGQGs and the optimized composite pulses (green dashed lines).

operator is

$$U_{g,\text{opt}}(T) = U(T, T_4)U(T_4, T_3)U(T_3, T_2)U(T_2, T_1)U(T_1, 0) = e^{i\gamma\vec{n}\cdot\vec{\sigma}}, \quad (16)$$

which is equivalent to the conventional NGQG in Eq. (9).

$$H_i(t) = \sum_{m=0}^2 \left(m\omega - \frac{m(m-1)}{2}\alpha \right) |m\rangle\langle m| + \frac{1}{2} \sum_{n=1,2} \left\{ \Omega(t) \exp \left[i \left(\int_0^t \omega(t') dt' - \varphi(t) \right) \right] \sqrt{n} |n-1\rangle\langle n| + \text{H.c.} \right\}. \quad (18)$$

Here ω is the intrinsic frequency, α is the anharmonicity of the transmon qubit, and $\Omega(t)$, $\omega(t)$, and $\varphi(t)$ represent the strength, frequency, and phase of the driving microwave field, respectively. In this work we consider the two lowest energy levels $|0\rangle$ and $|1\rangle$ as our qubit basis.

As shown in Fig. 1(a), the total evolution path for the optimized geometric gate is divided into five parts, which enclose the evolution loop $A \rightarrow B \rightarrow C \rightarrow B \rightarrow D \rightarrow E \rightarrow D \rightarrow A$. Compared with the conventional NGQG, the first and the last paths are the same. Accordingly, the azimuthal angles are similar. In addition, the original second path $B \rightarrow D$ is further divided into $B \rightarrow C \rightarrow B \rightarrow D \rightarrow E \rightarrow D$. The related azimuthal angles in these parts are

$$\phi(t) = \begin{cases} \phi_0 + \gamma + \pi, & B \rightarrow C \\ \phi_0 + \gamma + \pi, & C \rightarrow B \\ \phi_0 + \gamma, & B \rightarrow D \\ \phi_0 + \gamma + \pi, & D \rightarrow E \\ \phi_0 + \gamma + \pi, & E \rightarrow D. \end{cases} \quad (17)$$

Since $\phi(t)$ remains constant (except for the north pole B and the south pole D) during the evolution, the accumulated dynamical phase is zero. Also, there are no unwanted extra dynamical phase factors accumulated for the first and the final evolution paths.

From Figs. 2(a)–2(c) we can see that the optimized geometric gate (green dashed lines) can substantially improve the robustness against the detuning error when compared to the dynamical gate. For the H and S operations, it can outperform both the conventional and conventional 2 NGQGs, and the improvement becomes remarkable when the error is large. Surprisingly, for the Rabi error, it still performs better than the dynamical gate, as seen in Figs. 3(a)–3(c). By contrast, the fidelity of the conventional 2 NGQG would decrease drastically as the Rabi error increases. In other words, the optimized geometric gates can mitigate both types of errors for the dynamical gate at the same time. On the other hand, compared to its counterparts, the evolution time for the optimized geometric gate is prolonged. Whether it can still offer fidelity improvement considering the decoherence effect in the real experimental environment remains to be verified. This is considered further in Sec. III.

III. PHYSICAL IMPLEMENTATION

In this section we demonstrate the error-resilient character of our optimized geometric gates based on the transmon qubit in a superconducting circuit [28,42,46].

A. Single-qubit gate

The energy-level diagram of the transmon qubit is shown in Fig. 1(d), whose Hamiltonian can be described as

Note that, due to the weak anharmonicity in transmons, the quantum states would leak to the third-level state $|2\rangle$, as shown in Fig. 1(d). In order to combat this unwanted leakage error, in this work we use the derivative removal by adiabatic gate technique [63–65], where the pulse shape is designed as the

sinusoidal-like form

$$\Omega(t) = \Omega_{\max} \sin^2(\pi t/T). \quad (19)$$

Here the constant Ω_{\max} is the largest strength of the microwave field and T is the total evolution time for a given gate operation. When the frequency of the microwave field matches ω , namely, is on resonance, $H_t(t)$ is equivalent to Eq. (1) when ignoring the rotating-wave approximation and leakage effects. When considering the control errors, in our simulation, we take the Rabi error as $(1 + \epsilon)\Omega_{\max}$. Here ϵ relates to the inaccurate control of the Rabi frequency of the microwave field. For the detuning error, it is slightly different from the two-level case. For the transmon qubits with three levels, the qubit-frequency drift introduces detuning error as $\Omega_{\max}(\delta|1\rangle\langle 1| + 2\delta|2\rangle\langle 2|)$. Ignoring the third-level state $|2\rangle$, it is then equivalent to the form in Eq. (12).

To simulate the real environment in the transmon qubit, we use the Lindblad master equation [66] to numerically verify the gate robustness under decoherence,

$$\dot{\rho}_1 = -i[H_t(t), \rho_1] + \sum_{j=1}^2 \left(\frac{\kappa_j^-}{2} \mathcal{L}(\sigma_j) + \frac{\kappa_z^j}{2} \mathcal{L}(\chi_j) \right), \quad (20)$$

where ρ_1 is the density matrix of the transmon qubit, $\sigma_j = \sqrt{j}|j-1\rangle\langle j|$ is the standard lower operator, $\chi_j = |j\rangle\langle j|$ is the projector for the j th energy level, $\mathcal{L}(G) = 2G\rho_1 G^\dagger - G^\dagger G\rho_1 - \rho_1 G^\dagger G$ is the Lindblad operator for the operator G , and κ_j^- and κ_z^j are the relaxation and dephasing rates of the transmon, respectively. In our simulation, we choose the parameters of the decoherence rates from the state-of-the-art experiments, $\kappa_1^- = \kappa_2^- = \frac{1}{2}\kappa_z^1 = \frac{1}{2}\kappa_z^2 = \kappa = 2\pi \times 4$ kHz [67,68].

In the simulation, the parameters for the optimized geometric gate are $(\theta_S, \gamma_S) = (\pi, \pi/4)$, $(\theta_T, \gamma_T) = (\pi, \pi/8)$, and $(\theta_H, \gamma_H) = (\pi/4, \pi/2)$ for the S , T , and H gates, respectively, with $\phi_S = \phi_T = \phi_H = 0$. On the other hand, to achieve a good performance for the gate, we set $\alpha = 2\pi \times 320$ MHz, with $\Omega_{\max} = 2\pi \times \{43, 58, 58\}$ MHz for the $\{H, S, T\}$ gates, respectively. With the above parameter settings, we obtain the gate fidelity as $F_H = 99.90\%$, $F_S = 99.92\%$, and $F_T = 99.92\%$. The gate robustness of the optimized geometric gates considering decoherence is shown in Figs. 2(d)–2(f) and 3(d)–3(f). One can see that even though the performance for the optimized geometric gates slightly decreases due to long evolution time, these gates still outperform their counterparts. To further reveal the performance of the gates, in Fig. 5 we plot the fidelity for the H gate as a function of the detuning (Rabi) errors and decoherence rate. It is shown that the optimized geometric gate can substantially improve the gate fidelity for a rather wide range of decoherence rate κ and errors δ and ϵ .

B. Two-qubit gate

Here we discuss how to realize an optimized geometric entangling gate for the transmon qubits. The two-qubit gate can be constructed through two capacitively coupled transmon qubits by parametric modulation [69–71]. The Hamiltonian

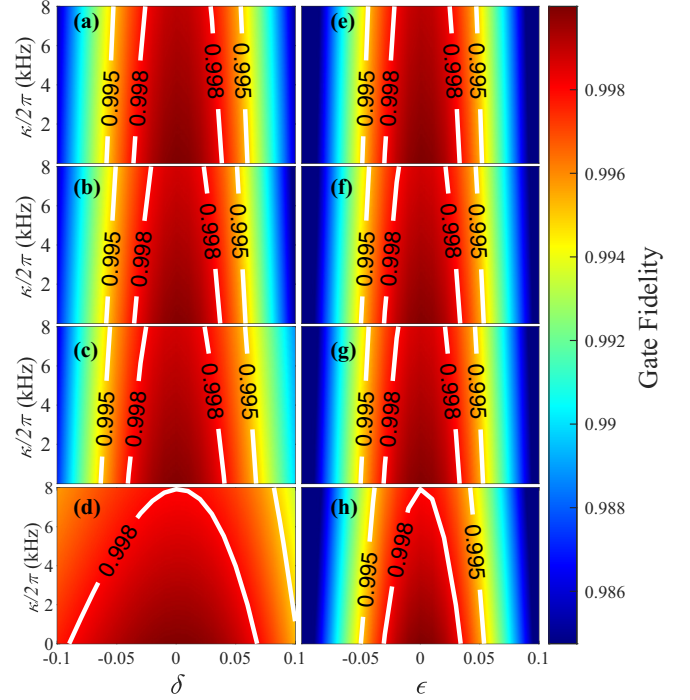


FIG. 5. Fidelity of the H gate as a function of decoherence and (a)–(d) detuning error and (e)–(h) Rabi error for (a) and (e) dynamical gates, (b) and (f) the conventional NGQG, (c) and (g) the conventional 2 NGQG, and (d) and (h) the optimized geometric gate.

for the coupled system is

$$H_c = \sum_{i=A,B} \sum_{k=0}^2 \left(k\omega_i - \frac{k(k-1)}{2} \alpha_i \right) |k\rangle_i \langle k| + g_{AB} \left(\sum_{m=0}^1 \sqrt{m+1} |m\rangle_A \langle m+1| \otimes \sum_{n=0}^1 \sqrt{n+1} |n+1\rangle_B \langle n| + \text{H.c.} \right), \quad (21)$$

where A and B denote the transmon qubits A and B , respectively, and g_{AB} is the qubit-qubit coupling strength between the two transmon qubits A and B . Applying a well-controlled microwave $\omega_A(t) = \omega_A + \hat{F}(t)$ to the first transmon qubit A , where $F(t) = \epsilon_L \cos(\nu_1 t + \eta)$, the Hamiltonian in the interaction picture is

$$H_I(t) = g_{AB} (|10\rangle\langle 01| e^{i\Delta_1 t} e^{-i\beta_1 \cos(\nu_1 t + \eta)} + \sqrt{2}|11\rangle\langle 02| e^{i(\Delta_1 + \alpha_B)t} e^{-i\beta_1 \cos(\nu_1 t + \eta)} + \sqrt{2}|20\rangle\langle 11| e^{i(\Delta_1 - \alpha_A)t} e^{-i\beta_1 \cos(\nu_1 t + \eta)} + \text{H.c.}), \quad (22)$$

where $\Delta_1 = \omega_A - \omega_B$ is the frequency difference between the two qubits and $\beta_1 = \epsilon_L / \nu_1$. As shown in Fig. 1(e), this Hamiltonian can introduce a transition in the single-excitation subspace $|10\rangle \leftrightarrow |01\rangle$; it can also introduce transitions in the double-excitation subspace $|02\rangle \leftrightarrow |11\rangle$ and $|11\rangle \leftrightarrow |20\rangle$. By meeting the resonance condition $\Delta_1 = \nu_1$, one can choose

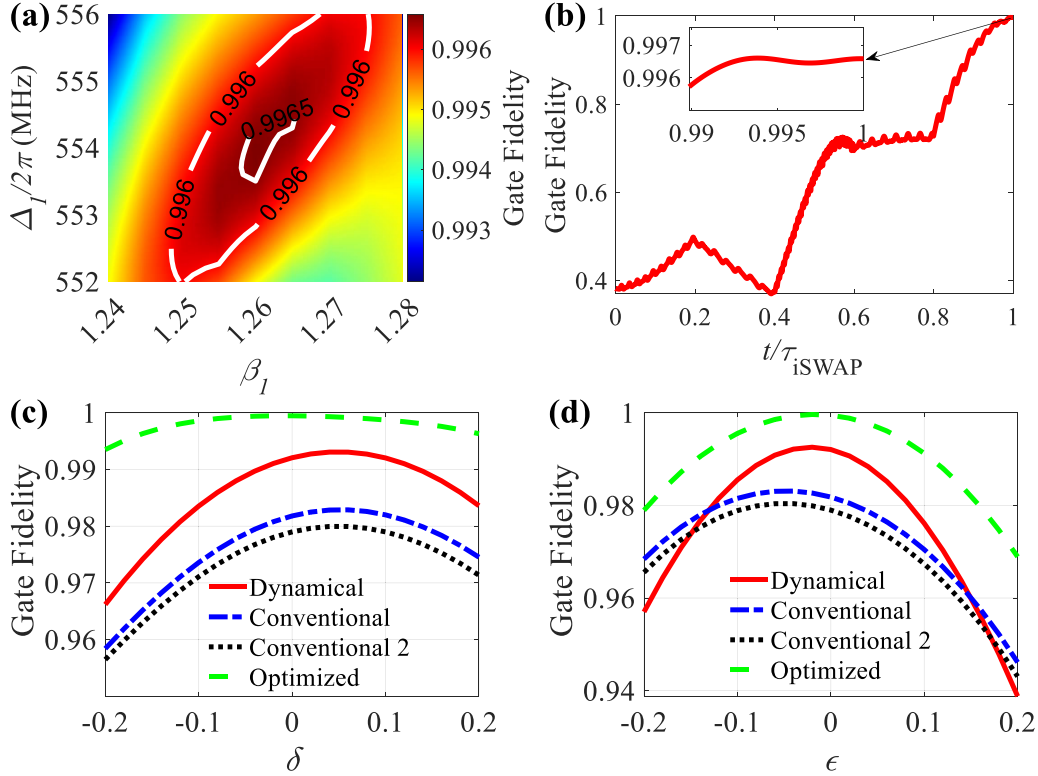


FIG. 6. Physical implementation of the iSWAP gate in superconducting transmon qubits. (a) The iSWAP gate as a function of the tunable parameters Δ_1 and β_1 . (b) Evolution of the gate fidelity of the optimized iSWAP gate as a function of time. (c) and (d) Gate fidelity for the detuning and Rabi errors without decoherence effects. Note that all of the above simulation results are based on the full Hamiltonian in Eq. (22).

the single-excitation subspace. Alternatively, by matching $v_1 = \Delta_1 + \alpha_B$ or $v_1 = \Delta_1 - \alpha_A$, one can also pick up the double-excitation subspace. In this work we focus on the single-excitation subspace. To simplify the Hamiltonian, we use the Jacobi-Anger identity

$$\begin{aligned} & \exp[-i\beta_1 \cos(v_1 t + \eta)] \\ &= \sum_{k=-\infty}^{\infty} (-i)^k J_k(\beta_1) \exp[-ik(v_1 t + \eta)], \end{aligned} \quad (23)$$

where $J_{-k}(\beta_1) = (-1)^k J_k(\beta_1)$, with $J_k(\beta_1)$ Bessel functions of the first kind. Neglecting the high-order oscillating terms by the rotating-wave approximation, the effective resonant interaction Hamiltonian in the single-excitation subspace $\{|10\rangle, |01\rangle\}$ can be written as

$$H'_I(t) = \frac{1}{2} g'_{AB} (|10\rangle\langle 01| e^{-i(\eta+\pi/2)} + \text{H.c.}). \quad (24)$$

Here $g'_{AB} = 2J_1(\beta_1)g_{AB}$ is the effective coupled strength which can be modulated by changing the value of β_1 . Similar to the single-qubit case, one can implement the optimized two-qubit geometric gates in the single-excitation subspace $\{|10\rangle, |01\rangle\}$, which can also be regarded as an effective two-level system. Specifically, the parameters are

$$\begin{aligned} g'_{AB}\tau_1 &= \vartheta, & \eta &\equiv \xi - \pi, & t &\in [0, \tau_1], \\ g'_{AB}(\tau_2 - \tau_1) &= \frac{\pi}{3}, & \eta &\equiv \xi + \gamma' + \pi, & t &\in [\tau_1, \tau_2], \end{aligned}$$

$$g'_{AB}(\tau_3 - \tau_2) = \frac{5\pi}{3}, \quad \eta \equiv \xi + \gamma', \quad t \in [\tau_2, \tau_3],$$

$$g'_{AB}(\tau_4 - \tau_3) = \frac{\pi}{3}, \quad \eta \equiv \xi + \gamma' + \pi, \quad t \in [\tau_3, \tau_4],$$

$$g'_{AB}(\tau - \tau_4) = \pi - \vartheta, \quad \eta \equiv \xi - \pi, \quad t \in [\tau_4, \tau]. \quad (25)$$

Here, by setting $\vartheta = \gamma' = \pi/2$ and $\xi = 0$, we can realize an iSWAP gate. Alternatively, one can also obtain the iSWAP gate in the dynamical way or just design it using the typical NGQG scheme [42,46].

We further consider the performance of the designed optimized iSWAP gate. In our simulation, the parameters are set as $g_{AB} = 2\pi \times 13.6$ MHz, $\alpha_A = 2\pi \times 320$ MHz, and $\alpha_B = 2\pi \times 343$ MHz. Below, we first consider the fidelity of our optimized iSWAP gate as a function of the tunable parameters Δ_1 and β_1 . The simulation results in Fig. 6(a) show that the optimized iSWAP gate can reach a high fidelity of more than 99.60% with the decoherence rate $\kappa = 2\pi \times 4$ kHz. As shown in Fig. 6(b), when taking $\beta_1 = 1.26$ and $\Delta_1 = 2\pi \times 554$ MHz, the gate fidelity can be as high as 99.66% with the same decoherence rate $\kappa = 2\pi \times 4$ kHz. Note that all of the above simulation results are based on the full Hamiltonian in Eq. (22).

To further verify the robustness of the optimized geometric iSWAP gate, we take both types of errors into account. The detuning error comes from the qubit-frequency drifts of the two qubits. This would change the resonance condition as $\Delta_1 \rightarrow \Delta_1 + \delta g'_{AB}$. The effective Rabi error ϵ affects the effective coupling strength that can be modeled as $g'_{AB} \rightarrow (1 + \epsilon)g'_{AB}$.

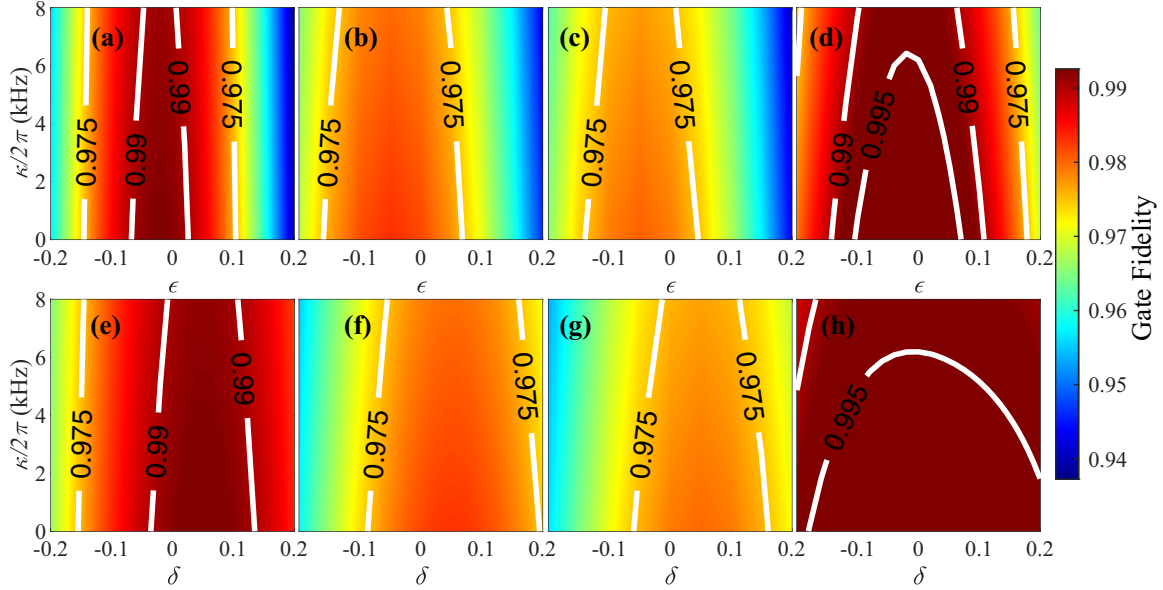


FIG. 7. Fidelity of the iSWAP gate as a function of the decoherence rate and (a)–(d) Rabi error and (e)–(h) detuning error for the (a) and (e) dynamical gates, (b) and (f) conventional NGQG, (c) and (g) conventional 2 NGQGs, and (d) and (h) optimized geometric gates. Note that all of the above simulation results are based on the Hamiltonian in Eq. (22).

As we can see in Figs. 6(c) and 6(d), without considering the decoherence effect, the fidelity for the optimized iSWAP gate can greatly surpass its counterparts for both types of errors in the whole region considered. In addition, we further analyze the gate performance by taking both the decoherence and error effects into account. The contour plot results are shown in Fig. 7. Compared to other types of gates, our designed scheme can realize fidelity higher than 99% in a rather wide region of decoherence rate and errors, which faithfully verifies the superiority of our optimized geometric gate.

IV. CONCLUSION

In this work we have proposed a general scheme to implement the optimized geometric gate based on composite pulses. The key to realizing the optimized geometric gate is to refine the evolution path which is robust to the detuning error. Meanwhile, the dynamical phase during the evolution is not accumulated. To this end, we established a set of optimized composite pulses, which helps enclose cyclic evolution for the geometric gate even though the detuning error exists. The numerical simulation results show that the obtained optimized geometric gate can mitigate both the Rabi and detuning errors at the same time with or without the presence of the decoherence effect. All these results indicate that our scheme provides a promising approach to improve conventional NGQGs and achieve high-fidelity quantum computation.

ACKNOWLEDGMENTS

This work was supported by the National Natural Science Foundation of China (Grants No. 11905065, No. 62171144, and No. 12305019) and the Natural Science Foundation of Guangxi (Grants No. AD22035186 and No. 2021GXNS-FAA220011).

APPENDIX A: ERROR ROBUSTNESS ANALYSIS FOR OTHER TYPES OF GATES

In the main text we demonstrated the robustness of the universal gate set $\{H, S, T\}$ for our optimized geometric gate. To fully verify its performance, here we further discuss the case for the \hat{x} -axis rotation, which is useful for randomized benchmarking in experiments. By performing a Taylor series expansion of the fidelity, we can analytically compare the robustness performance for various gates. Here the fidelity is defined as $F = \text{Tr}(V^\dagger U)/2$, where V is the ideal target rotation and U is the actual rotation. For the Rabi error, we can expand the fidelity of the gates as

$$\begin{aligned} \mathcal{F}_{\text{dyn}}^\epsilon(\hat{x}, \gamma) &\simeq 1 - \frac{\gamma^2}{8}\epsilon^2 + O(\epsilon^3), \\ \mathcal{F}_{\text{con}}^\epsilon(\hat{x}, \gamma) &\simeq 1 - \frac{\pi^2}{2}\sin^4\left(\frac{\gamma}{4}\right)\epsilon^2 + O(\epsilon^3), \\ \mathcal{F}_{\text{con},2}^\epsilon(\hat{x}, \gamma) &\simeq 1 - \frac{\pi^2}{2}\cos^4\left(\frac{\gamma}{4}\right)\epsilon^2 + O(\epsilon^3), \\ \mathcal{F}_{\text{opt}}^\epsilon(\hat{x}, \gamma) &\simeq 1 - \frac{\pi^2}{2}\sin^4\left(\frac{\gamma}{4}\right)\epsilon^2 + O(\epsilon^3). \end{aligned} \quad (\text{A1})$$

Here $\mathcal{F}_{\text{dyn}}^\epsilon(\hat{x}, \gamma)$, $\mathcal{F}_{\text{con}}^\epsilon(\hat{x}, \gamma)$, $\mathcal{F}_{\text{con},2}^\epsilon(\hat{x}, \gamma)$, and $\mathcal{F}_{\text{opt}}^\epsilon(\hat{x}, \gamma)$ denote the fidelity of the \hat{x} -axis rotation around the angle γ for the dynamical gate, the conventional geometric gate, the conventional 2 geometric gate in Refs. [46,47], and our optimized geometric gate, respectively. In the region $-\pi \leq \gamma \leq \pi$, we can easily demonstrate the relations $\mathcal{F}_{\text{con},2}^\epsilon(\hat{x}, \gamma) \leq \mathcal{F}_{\text{dyn}}^\epsilon(\hat{x}, \gamma)$, $\mathcal{F}_{\text{dyn}}^\epsilon(\hat{x}, \gamma) \leq \mathcal{F}_{\text{con}}^\epsilon(\hat{x}, \gamma)$, and $\mathcal{F}_{\text{con}}^\epsilon(\hat{x}, \gamma) \leq \mathcal{F}_{\text{opt}}^\epsilon(\hat{x}, \gamma)$, which means that the dynamical gate is sensitive to the Rabi error when compared to the conventional geometric and optimized geometric gates. In addition, we find $\mathcal{F}_{\text{con}}^\epsilon(\hat{x}, \gamma) = \mathcal{F}_{\text{opt}}^\epsilon(\hat{x}, \gamma)$, namely, our optimized geometric

gate has the same robustness as the conventional geometric gate against the Rabi error.

For the detuning error, we can expand the fidelity as

$$\begin{aligned}\mathcal{F}_{\text{dyn}}^{\delta}(\hat{x}, \gamma) &\simeq 1 + \frac{1}{4}[\cos(\gamma) - 1]\delta^2 + O(\delta^3), \\ \mathcal{F}_{\text{con}}^{\delta}(\hat{x}, \gamma) &\simeq 1 - 2\cos^4\left(\frac{\gamma}{4}\right)\delta^2 + O(\delta^3), \\ \mathcal{F}_{\text{con},2}^{\delta}(\hat{x}, \gamma) &\simeq 1 - 2\sin^4\left(\frac{\gamma}{4}\right)\delta^2 + O(\delta^3), \\ \mathcal{F}_{\text{opt}}^{\delta}(\hat{x}, \gamma) &\simeq 1 + \frac{1}{4}[-\cos(\gamma) - 1]\delta^2 + O(\delta^3).\end{aligned}\quad (\text{A2})$$

From Eqs. (A2), in the region $-\pi \leq \gamma \leq \pi$, we have the relations $\mathcal{F}_{\text{con}}^{\delta}(\hat{x}, \gamma) \leq \mathcal{F}_{\text{dyn}}^{\delta}(\hat{x}, \gamma)$, $\mathcal{F}_{\text{dyn}}^{\delta}(\hat{x}, \gamma) \leq \mathcal{F}_{\text{con},2}^{\delta}(\hat{x}, \gamma)$, and $\mathcal{F}_{\text{con}}^{\delta}(\hat{x}, \gamma) \leq \mathcal{F}_{\text{opt}}^{\delta}(\hat{x}, \gamma)$. These results suggest that the conventional geometric gate is more sensitive than the dynamical counterpart and our optimized geometric gate performs better than the conventional geometric gate. However, when comparing the optimized geometric gate with the dynamical gate and the conventional 2 geometric gate, the case becomes a little complex. In the range $|\gamma| \in [\pi/2, \pi]$ we find $\mathcal{F}_{\text{dyn}}^{\delta}(\hat{x}, \gamma) \leq \mathcal{F}_{\text{opt}}^{\delta}(\hat{x}, \gamma)$, while in the region $|\gamma| \in [2\pi/3, \pi]$ we have $\mathcal{F}_{\text{con},2}^{\delta}(\hat{x}, \gamma) \leq \mathcal{F}_{\text{opt}}^{\delta}(\hat{x}, \gamma)$. This means that our optimized geometric gate can only tolerate effects for a specific region. The case for the \hat{y} -axis rotation is similar.

APPENDIX B: DEMONSTRATION OF ZERO DYNAMICAL PHASE ACCUMULATION NEAR THE NORTH AND SOUTH POLES

As shown in Eqs. (11) and (17), the azimuthal angle $\phi(t)$ at the north pole B and the south pole D is not continuous. At these points, the derivatives $\dot{\phi}(t)$ are not zero since $\phi(t)$ abruptly changes. To calculate the dynamical phase, we should use Eq. (7a), i.e., the definition of the dynamical phase. Below we demonstrate that even though $\phi(t)$ jumps at these points, the dynamical phase accumulated is still zero.

We take the north pole as an example. First, we assume there is a infinitesimal jump time δt with $\lim \delta t = 0$. Suppose the Hamiltonian before and after jumping within the time

interval $[t - \delta t, t + \delta t]$ is

$$\begin{aligned}\mathcal{H}(t \pm \delta t) &= \frac{\Omega(t \pm \delta t)}{2}[\cos \varphi(t \pm \delta t)\sigma_x + \sin \varphi(t \pm \delta t)\sigma_y] \\ &= \frac{\Omega(t')}{2}[\cos \varphi(t')\sigma_x + \sin \varphi(t')\sigma_y].\end{aligned}\quad (\text{B1})$$

Here $t' = t \pm \delta t$ denotes the time before and after the jumping. On the other hand, the polar angle at the north pole remains unchanged, i.e., $\theta = 0$ before and after jumping. Therefore, the dressed state at the north pole is thus

$$|\Psi_{+}(t \pm \delta t)\rangle = e^{i\phi(t \pm \delta t)}|0\rangle = e^{i\phi(t')}|0\rangle.\quad (\text{B2})$$

Then, during the jumping interval, the dynamical phase accumulated can be calculated by inserting $\mathcal{H}(t \pm \delta t)$ and $|\Psi_{+}(t \pm \delta t)\rangle$ into Eq. (7a), for which we find

$$\gamma'_d = \gamma_d^{t-\delta t} + \gamma_d^{t+\delta t},\quad (\text{B3})$$

where

$$\begin{aligned}\gamma_d^{t-\delta t} &= -\int_{t'-\delta t}^{t'} \langle \Psi_{+}(t - \delta t) | \mathcal{H}(t - \delta t) | \Psi_{+}(t - \delta t) \rangle dt, \\ \gamma_d^{t+\delta t} &= -\int_{t'}^{t'+\delta t} \langle \Psi_{+}(t + \delta t) | \mathcal{H}(t + \delta t) | \Psi_{+}(t + \delta t) \rangle dt.\end{aligned}\quad (\text{B4})$$

Specifically, the related antiderivative is

$$\begin{aligned}&\int \langle \Psi_{+}(t \pm \delta t) | \mathcal{H}(t \pm \delta t) | \Psi_{+}(t \pm \delta t) \rangle dt \\ &= \int e^{-i\phi(t')} \langle 0 | \frac{\Omega(t')}{2} [\cos \varphi(t')\sigma_x + \sin \varphi(t')\sigma_y] e^{i\phi(t')} | 0 \rangle dt \\ &= \int \frac{\Omega(t')}{2} \langle 0 | [\cos \varphi(t')\sigma_x + \sin \varphi(t')\sigma_y] | 0 \rangle dt \\ &= \int \frac{\Omega(t')}{2} [\cos \varphi(t')\langle 0 | 1 \rangle + i \sin \varphi(t')\langle 0 | 1 \rangle] dt \\ &= 0.\end{aligned}\quad (\text{B5})$$

Thus we have

$$\gamma'_d = \gamma_d^{t-\delta t} + \gamma_d^{t+\delta t} = 0,\quad (\text{B6})$$

namely, during the jumping interval δt , the dynamical phase accumulated is still zero. The case for the south pole can be understood in the same way.

-
- [1] Y. Ota and Y. Kondo, *Phys. Rev. A* **80**, 024302 (2009).
[2] B. T. Torosov and N. V. Vitanov, *Phys. Rev. A* **90**, 012341 (2014).
[3] H. L. Gevorgyan and N. V. Vitanov, *Phys. Rev. A* **104**, 012609 (2021).
[4] C. Zhang, R. E. Throckmorton, X.-C. Yang, X. Wang, E. Barnes, and S. Das Sarma, *Phys. Rev. Lett.* **118**, 216802 (2017); B.-B. Liu, F.-Q. Guo, L.-L. Yan, S. Zhang, M. Feng, and S.-L. Su, *Adv. Quantum Technol.* **4**, 2100093 (2021).
[5] A. Carlini and T. Koike, *Phys. Rev. A* **86**, 054302 (2012).
[6] J. Geng, Y. Wu, X. Wang, K. Xu, F. Shi, Y. Xie, X. Rong, and J. Du, *Phys. Rev. Lett.* **117**, 170501 (2016).
[7] Y. Dong, C. Feng, Y. Zheng, X.-D. Chen, G.-C. Guo, and F.-W. Sun, *Phys. Rev. Res.* **3**, 043177 (2021).
[8] L.-N. Sun, L.-L. Yan, S.-L. Su, and Y. Jia, *Phys. Rev. Appl.* **16**, 064040 (2021).
[9] G. Tang, X.-Y. Yang, Y. Yan, and J. Lu, *Phys. Lett. A* **449**, 128349 (2022).
[10] Y. Liang, P. Shen, T. Chen, and Z.-Y. Xue, *Sci. China Inf. Sci.* **66**, 180502 (2023).
[11] W. Dong, F. Zhuang, S. E. Economou, and E. Barnes, *PRX Quantum* **2**, 030333 (2021).
[12] E. Barnes, F. A. Calderon-Vargas, W. Dong, B. Li, J. Zeng, and F. Zhuang, *Quantum Sci. Technol.* **7**, 023001 (2022).

- [13] H. L. Tang, K. Connelly, A. Warren, F. Zhuang, S. E. Economou, and E. Barnes, *Phys. Rev. Appl.* **19**, 044094 (2023).
- [14] H. T. Nelson, E. Piliouras, K. Connelly, and E. Barnes, *Phys. Rev. A* **108**, 012407 (2023).
- [15] P. Zanardi and M. Rasetti, *Phys. Lett. A* **264**, 94 (1999).
- [16] J. Pachos, P. Zanardi, and M. Rasetti, *Phys. Rev. A* **61**, 010305(R) (1999).
- [17] F. Wilczek and A. Zee, *Phys. Rev. Lett.* **52**, 2111 (1984).
- [18] J. Anandan, *Phys. Lett. A* **133**, 171 (1988).
- [19] M. V. Berry, *Proc. R. Soc. London Ser. A* **392**, 45 (1984).
- [20] Y. Aharonov and J. Anandan, *Phys. Rev. Lett.* **58**, 1593 (1987).
- [21] J. Samuel and R. Bhandari, *Phys. Rev. Lett.* **60**, 2339 (1988).
- [22] J. A. Jones, V. Vedral, A. Ekert, and G. Castagnoli, *Nature (London)* **403**, 869 (2000).
- [23] L.-M. Duan, J. I. Cirac, and P. Zoller, *Science* **292**, 1695 (2001).
- [24] W. Xiang-Bin and M. Keiji, *Phys. Rev. Lett.* **87**, 097901 (2001).
- [25] S.-L. Zhu and Z. D. Wang, *Phys. Rev. Lett.* **89**, 097902 (2002).
- [26] A. A. Abdumalikov, Jr., J. M. Fink, K. Juliusson, M. Pechal, S. Berger, A. Wallraff, and S. Filipp, *Nature (London)* **496**, 482 (2013).
- [27] Y. Xu, W. Cai, Y. Ma, X. Mu, L. Hu, T. Chen, H. Wang, Y. P. Song, Z.-Y. Xue, Z.-Q. Yin, and L. Sun, *Phys. Rev. Lett.* **121**, 110501 (2018).
- [28] Y. Xu, Z. Hua, T. Chen, X. Pan, X. Li, J. Han, W. Cai, Y. Ma, H. Wang, Y. P. Song, Z.-Y. Xue, and L. Sun, *Phys. Rev. Lett.* **124**, 230503 (2020).
- [29] P. Zhao, Z. Dong, Z. Zhang, G. Guo, D. Tong, and Y. Yin, *Sci. China Phys. Mech. Astron.* **64**, 250362 (2021).
- [30] X.-X. Yang, L.-L. Guo, H.-F. Zhang, L. Du, C. Zhang, H.-R. Tao, Y. Chen, P. Duan, Z.-L. Jia, W.-C. Kong, and G.-P. Guo, *Phys. Rev. Appl.* **19**, 044076 (2023).
- [31] M.-Z. Ai, S. Li, Z. Hou, R. He, Z.-H. Qian, Z.-Y. Xue, J.-M. Cui, Y.-F. Huang, C.-F. Li, and G.-C. Guo, *Phys. Rev. Appl.* **14**, 054062 (2020).
- [32] M.-Z. Ai, S. Li, R. He, Z.-Y. Xue, J.-M. Cui, Y.-F. Huang, C.-F. Li, and G.-C. Guo, *Fundam. Res.* **2**, 661 (2022).
- [33] C. Zu, W.-B. Wang, L. He, W.-G. Zhang, C.-Y. Dai, F. Wang, and L.-M. Duan, *Nature (London)* **514**, 72 (2014).
- [34] B. B. Zhou, P. C. Jerger, V. O. Shkolnikov, F. J. Heremans, G. Burkard, and D. D. Awschalom, *Phys. Rev. Lett.* **119**, 140503 (2017).
- [35] K. Nagata, K. Kuramitani, Y. Sekiguchi, and H. Kosaka, *Nat. Commun.* **9**, 3227 (2018).
- [36] J. Du, P. Zou, and Z. D. Wang, *Phys. Rev. A* **74**, 020302(R) (2006).
- [37] G. Feng, G. Xu, and G. Long, *Phys. Rev. Lett.* **110**, 190501 (2013).
- [38] Z. Zhu, T. Chen, X. Yang, J. Bian, Z.-Y. Xue, and X. Peng, *Phys. Rev. Appl.* **12**, 024024 (2019).
- [39] S.-L. Zhu and Z. D. Wang, *Phys. Rev. A* **67**, 022319 (2003).
- [40] X.-D. Zhang, S.-L. Zhu, L. Hu, and Z. D. Wang, *Phys. Rev. A* **71**, 014302 (2005).
- [41] P. Z. Zhao, X.-D. Cui, G. F. Xu, E. Sjöqvist, and D. M. Tong, *Phys. Rev. A* **96**, 052316 (2017).
- [42] T. Chen and Z.-Y. Xue, *Phys. Rev. Appl.* **10**, 054051 (2018).
- [43] C. Zhang, T. Chen, S. Li, X. Wang, and Z.-Y. Xue, *Phys. Rev. A* **101**, 052302 (2020).
- [44] L.-N. Ji, C.-Y. Ding, T. Chen, and Z.-Y. Xue, *Adv. Quantum Technol.* **4**, 2100019 (2021).
- [45] M.-J. Liang and Z.-Y. Xue, *Phys. Rev. A* **106**, 012603 (2022).
- [46] J. Zhou, S. Li, G.-Z. Pan, G. Zhang, T. Chen, and Z.-Y. Xue, *Phys. Rev. A* **103**, 032609 (2021).
- [47] C. Zhang, T. Chen, X. Wang, and Z.-Y. Xue, *Adv. Quantum Technol.* **4**, 2100011 (2021).
- [48] L.-J. Guo, H. Xu, Z.-Y. Fang, T. Chen, K. Wei, and C. Zhang, *Phys. Rev. A* **107**, 012604 (2023).
- [49] B.-J. Liu, X.-K. Song, Z.-Y. Xue, X. Wang, and M.-H. Yung, *Phys. Rev. Lett.* **123**, 100501 (2019).
- [50] T. Chen and Z.-Y. Xue, *Phys. Rev. Appl.* **14**, 064009 (2020).
- [51] S. Li, J. Xue, T. Chen, and Z.-Y. Xue, *Adv. Quantum Technol.* **4**, 2000140 (2021).
- [52] C.-Y. Ding, L.-N. Ji, T. Chen, and Z.-Y. Xue, *Quantum Sci. Technol.* **7**, 015012 (2022).
- [53] T. Chen, Z.-Y. Xue, and Z. D. Wang, *Phys. Rev. Appl.* **18**, 014062 (2022).
- [54] Y. Liang, P. Shen, L.-N. Ji, and Z.-Y. Xue, *Phys. Rev. Appl.* **19**, 024051 (2023).
- [55] C.-Y. Ding, L. Chen, L.-H. Zhang, and Z.-Y. Xue, *Front. Phys.* **18**, 61304 (2023).
- [56] L. Viola, E. Knill, and S. Lloyd, *Phys. Rev. Lett.* **82**, 2417 (1999).
- [57] G. Xu and G. Long, *Phys. Rev. A* **90**, 022323 (2014).
- [58] X. Wu and P. Z. Zhao, *Phys. Rev. A* **102**, 032627 (2020).
- [59] X. Wu and P. Z. Zhao, *Front. Phys.* **17**, 31502 (2022).
- [60] K. Z. Li, P. Z. Zhao, and D. M. Tong, *Phys. Rev. Res.* **2**, 023295 (2020).
- [61] W. Li, *New J. Phys.* **23**, 073039 (2021).
- [62] Y.-H. Kang, Y.-H. Chen, X. Wang, J. Song, Y. Xia, A. Miranowicz, S.-B. Zheng, and F. Nori, *Phys. Rev. Res.* **4**, 013233 (2022).
- [63] F. Motzoi, J. M. Gambetta, P. Rebentrost, and F. K. Wilhelm, *Phys. Rev. Lett.* **103**, 110501 (2009).
- [64] J. M. Gambetta, F. Motzoi, S. T. Merkel, and F. K. Wilhelm, *Phys. Rev. A* **83**, 012308 (2011).
- [65] Z. Chen, J. Kelly, C. Quintana, R. Barends, B. Campbell, Y. Chen, B. Chiaro, A. Dunsworth, A. G. Fowler, E. Lucero, E. Jeffrey, A. Megrant, J. Mutus, M. Neeley, C. Neill, P. J. J. O'Malley, P. Roushan, D. Sank, A. Vainsencher, J. Wenner *et al.*, *Phys. Rev. Lett.* **116**, 020501 (2016).
- [66] G. Lindblad, *Commun. Math. Phys.* **48**, 119 (1976).
- [67] H.-L. Huang, D. Wu, D. Fan, and X. Zhu, *Sci. China Inf. Sci.* **63**, 180501 (2020).
- [68] M. Kjaergaard, M. E. Schwartz, J. Braumüller, P. Krantz, J. I.-J. Wang, S. Gustavsson, and W. D. Oliver, *Annu. Rev. Condens. Matter Phys.* **11**, 369 (2020).
- [69] M. Roth, M. Ganzhorn, N. Moll, S. Filipp, G. Salis, and S. Schmidt, *Phys. Rev. A* **96**, 062323 (2017).
- [70] S. A. Caldwell, N. Didier, C. A. Ryan, E. A. Sete, A. Hudson, P. Karalekas, R. Manenti, M. P. da Silva, R. Sinclair, E. Acala, N. Alidoust, J. Angeles, A. Bestwick, M. Block, B. Bloom, A. Bradley, C. Bui, L. Capelluto, R. Chilcott, J. Cordova *et al.*, *Phys. Rev. Appl.* **10**, 034050 (2018).
- [71] J. Chu, D. Li, X. Yang, S. Song, Z. Han, Z. Yang, Y. Dong, W. Zheng, Z. Wang, X. Yu, D. Lan, X. Tan, and Y. Yu, *Phys. Rev. Appl.* **13**, 064012 (2020).